

# Relativistic rotating vector model for X-ray millisecond pulsars

Juri Poutanen<sup>1, 2, 3</sup>

<sup>1</sup> Department of Physics and Astronomy, FI-20014 University of Turku, Finland  
e-mail: juri.poutanen@utu.fi

<sup>2</sup> Space Research Institute of the Russian Academy of Sciences, Profsoyuznaya str. 84/32, 117997 Moscow, Russia

<sup>3</sup> Nordita, KTH Royal Institute of Technology and Stockholm University, Roslagstullsbacken 23, 10691 Stockholm, Sweden

June 19, 2020

## ABSTRACT

X-ray radiation produced on the surface of accreting magnetized neutron stars is expected to be strongly polarized. Rotation of the polarization angle with pulsar phase gives a direct measure of the source inclination and magnetic obliquity. In case of rapidly rotating millisecond pulsars, the relativistic motion of the emission region causes additional rotation of the polarization plane. Here we develop relativistic rotating vector model, where we derive analytical expression for the polarization angle as a function of pulsar phase accounting also for aberration and gravitational light bending in Schwarzschild metric. We show that in the case of fast pulsars, and closeness of the inclination and magnetic obliquity, the rotation of polarization plane can reach tens of degrees, strongly influencing the observed shape of the polarization angle phase dependence. The rotation angle grows nearly linearly with the spin rate but is less sensitive to the neutron star radius. This angle is large even for large spots. Our results have implications for the modelling of X-ray polarization from accreting millisecond pulsars to be observed with the upcoming Imaging X-ray Polarimeter Explorer and the enhanced X-ray Timing and Polarimetry mission. X-ray polarization may improve constraints on the neutron star mass and radius coming from the pulse profile modelling.

**Key words.** methods: analytical – polarization – stars: neutron – stars: oscillations – X-rays: binaries

## 1. Introduction

Constraints on the equation of state (EoS) of cold dense matter can be obtained using astrophysical measurements of neutron star (NS) (Lattimer & Prakash 2007; Özel & Freire 2016; Watts et al. 2016, 2019; Miller et al. 2020). Precise timing of radio pulsars in binary systems (Lorimer 2008) constrained the maximum NS mass to be at least  $2M_{\odot}$  (Demorest et al. 2010; Antoniadis et al. 2013; Fonseca et al. 2016), which rules out very soft EoS. Determination of NS radii would narrow down the possible EoS and was a subject of numerous studies. For example, mass-radius relation can be obtained using spectral information on surface thermal emission during X-ray bursts (Özel et al. 2009; Steiner et al. 2010; Suleimanov et al. 2011; Steiner et al. 2013; Poutanen et al. 2014; Nättilä et al. 2016, 2017; Suleimanov et al. 2020), in quiescent states of NSs in binary systems (Rutledge et al. 1999; Heinke et al. 2003, 2006; Webb & Barret 2007; Guillot et al. 2013; Lattimer & Steiner 2014; Bogdanov et al. 2016; Steiner et al. 2018) as well as from central compact objects in supernova remnants (Ho & Heinke 2009; Klochkov et al. 2015; Suleimanov et al. 2017). Additional constraints come from tidal deformabilities measured using gravitational wave signal from merging NSs (Bauswein et al. 2017; Annala et al. 2018; Abbott et al. 2018; De et al. 2018; Most et al. 2018).

NS parameters can also be measured from the X-ray pulse profiles of accreting (Poutanen & Gierliński 2003; Leahy et al. 2008, 2009; Morsink & Leahy 2011; Salmi et al. 2018), nuclear (Bhattacharyya et al. 2005; Lo et al. 2013; Miller & Lamb 2015; Stevens et al. 2016) and radio millisecond pulsars (Bogdanov et al. 2008; Bogdanov 2013; Bogdanov et al. 2019; Miller et al. 2019; Riley et al. 2019). In particular, the pulse

profiles produced by a hotspot on a NS surface are strongly affected by special as well as general relativistic effects such as Doppler effect, light bending and time delays, and therefore they carry information about NS radius and mass (Poutanen & Gierliński 2003; Poutanen & Beloborodov 2006; Cadeau et al. 2007; Morsink et al. 2007; Nättilä & Pihajoki 2018; Suleimanov et al. 2020). The magnetic field in these NSs is rather weak and does not affect the radiative transport allowing to theoretically predict the surface emission pattern and spectrum and the pulse profile reliably. However, similar light curves can be produced with a very different set of parameters, for example, there is a degeneracy in exchanging the observer inclination and the magnetic obliquity (Viironen & Poutanen 2004). A possible way to distinguish between the models and to improve the constraints on the masses and radii is to observe variations of the polarization degree (PD) and polarization angle (PA) with phase (Salmi et al. 2018). This kind of observations turned out to be a valuable tool in determining the geometry of the radio pulsar emission region (e.g. Blaskiewicz et al. 1991). For X-ray pulsars, polarimetric observations will be possible in the near future with the Imaging X-ray Polarimeter Explorer (IXPE) (Weisskopf et al. 2016) and the enhanced X-ray Timing and Polarimetry (eXTP) mission (Zhang et al. 2016, 2019).

For a slowly rotating star, the variations of polarization angle (PA, i.e. the electric vector position angle) with pulsar phase follow the projection of the hotspot normal on the sky as described by the rotating vector model (Radhakrishnan & Cooke 1969). However, when the source moves with velocity that is a significant fraction of the speed of light, the preferred direction of the electric vector rotates. A rather general expression for the rotation of the polarization plane in this case was obtained by Blandford & Königl (1979) and Lyutikov et al. (2003) and dis-

cussed recently by Lyutikov (2017) and Lyutikov & Kravchenko (2017). In the context of surface emission from NSs, the effect was considered by Ferguson (1973, 1976), but no explicit analytical expression was found. A more recent work by Lyutikov (2016) also addressed this issue in the context of radio pulsars. None of the quoted papers have included the effects related to light bending in the vicinity of a NS. Light bending was accounted for by Pavlov & Zavlin (2000) who considered the case of slowly rotating, strongly magnetized pulsars. Here we present relativistic rotating vector model that describes variations of the polarization plane of emission produced by a hotspot on the surface of a rapidly rotating NS accounting for the relativistic aberration and gravitational light bending. We consider here only spherical stars, but generalization to arbitrary NS shape is straightforward and will be considered elsewhere (Loktev et al., in prep.). The results of the current study were already used by Viironen & Poutanen (2004), but the derivation of the general expression was not presented there.

## 2. Radiation from antipodal spots

Let us consider a spherical NS of radius  $R$  and mass  $M$  and two identical antipodal hotspots at its surface displaced from the NS rotational axis. Due to stellar rotation, the visibility of the hotspots changes resulting in variations of the observed flux, PD and PA (i.e. position angle of the dominant electric field). The observed flux and the PD at a given pulsar phase  $\phi$  depends on the angle  $\alpha'$  between the momentum of emitted photon and the local normal to the stellar surface in the spot comoving frame. We assume that they do not depend on the azimuthal angle at which the spot is seen in the comoving frame, which is a good approximation for low magnetic field pulsars (see Pavlov & Zavlin 2000 for the high magnetic field case). Polarization degree is invariant and does not change along photon trajectory, thus the observed PD is equal to that measured in the comoving frame at the emitted energy  $E'$  and angle  $\alpha'$ . If we have a model how Stokes parameters depend on energy and angles in the spot comoving frame, we can then transform them to the observer frame. First, we make the Lorentz transformation to the non-rotating local frame accounting for Doppler boosting and relativistic aberration. Then we follow photon trajectories to the observer at infinity in Schwarzschild space-time. Deviations from the Schwarzschild metric due to the stellar rotation have a small effect (Braje et al. 2000) and are neglected here. We also need to account for the time delays which in the extreme cases of NS spinning at 600 Hz can reach 5–10 per cent of the pulsar period.

For completeness we first repeat the method to compute the observed flux (see also Poutanen & Beloborodov 2006; Salmi et al. 2018; Bogdanov et al. 2019; Suleimanov et al. 2020) and then extend it to the description of the PD (Sect. 2.2) and PA (in Sect. 3).

### 2.1. Light bending and time delay

Let  $i$  be the inclination of the spin axis to the line of sight and let us choose the coordinate system so that the unit vector in the direction to the observer is  $\hat{k} = (\sin i, 0, \cos i)$ , see Fig. 1 for the geometry. Let the magnetic obliquity, i.e. co-latitude of the primary hotspot, be  $\theta$ . The spot coordinates vary periodically with pulsar rotational phase  $\phi$  and the unit vector of the spot normal (which is parallel to the radius-vector of the emission point in case of a spherical star) is  $\hat{n} = (\sin \theta \cos \phi, \sin \theta \sin \phi, \cos \theta)$ .

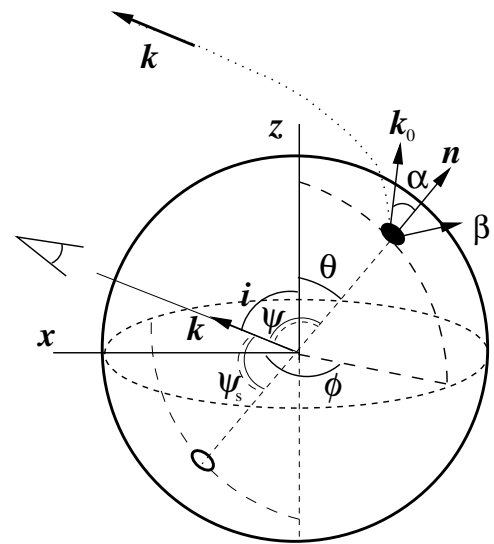


Fig. 1. Geometry of the problem.

Thus the angle between the direction to the spot and the line of sight is given by

$$\cos \psi \equiv \hat{k} \cdot \hat{n} = \cos i \cos \theta + \sin i \sin \theta \cos \phi, \quad (1)$$

where  $\phi = 0$  when the spot is closest to the observer. For the secondary spot we substitute  $\phi \rightarrow \phi + \pi$  and  $\theta \rightarrow \pi - \theta$ .

In Schwarzschild metric the photon orbits are planar and the original direction of the photon momentum near the stellar surface  $\hat{k}_0$  is related to its direction at infinity  $\hat{k}$  and the normal to the star  $\hat{n}$  (Poutanen & Gierliński 2003):

$$\hat{k}_0 = [\sin \alpha \hat{k} + \sin(\psi - \alpha) \hat{n}] / \sin \psi, \quad (2)$$

where  $\alpha$  is the angle between  $\hat{k}_0$  and  $\hat{n}$ ,  $\cos \alpha = \hat{k}_0 \cdot \hat{n}$ . The relation between angles  $\alpha$  and  $\psi$  can be obtained by computing an elliptical integral (Pechenick et al. 1983; Beloborodov 2002; Poutanen & Gierliński 2003; Poutanen & Beloborodov 2006; Salmi et al. 2018):

$$\psi = \int_R^\infty \frac{dr}{r^2} \left[ \frac{1}{b^2} - \frac{1}{r^2} \left( 1 - \frac{R_S}{r} \right) \right]^{-1/2}, \quad (3)$$

where  $R_S \equiv 2GM/c^2$  is the Schwarzschild radius of the NS and

$$b = \frac{R}{\sqrt{1-u}} \sin \alpha \quad (4)$$

is the impact parameter and  $u = R_S/R$  is the NS compactness. For our calculations here we use approximate analytical formula for the dependence  $\alpha(\psi)$  suggested by Poutanen (2019):

$$\cos \alpha \approx 1 - y(1-u)G(y,u), \quad (5)$$

where  $y = 1 - \cos \psi$ , and

$$G(y,u) = 1 + \frac{u^2 y^2}{112} - \frac{e}{100} u y \left[ \ln \left( 1 - \frac{y}{2} \right) + \frac{y}{2} \right]. \quad (6)$$

This approximation has a typical accuracy of 0.05% for a large range of emission angles and for most realistic NS compactnesses.

The spot velocity is described by the unit vector  $\hat{v} = (-\sin\phi, \cos\phi, 0)$  and the velocity amplitude

$$\beta = \frac{v}{c} = \frac{2\pi R}{c} \frac{\nu}{\sqrt{1-u}} \sin\theta, \quad (7)$$

where the observed pulsar frequency  $\nu$  is corrected for the redshift  $\sqrt{1-u}$ . The angle between the velocity and the photon direction is then

$$\cos\xi = \hat{v} \cdot \hat{k}_0 = \frac{\sin\alpha}{\sin\psi} \hat{v} \cdot \hat{k} = -\frac{\sin\alpha}{\sin\psi} \sin i \sin\phi. \quad (8)$$

The unit vector of the photon momentum in the spot comoving frame can be obtained from the Lorentz transformation

$$\hat{k}'_0 = \delta [\hat{k}_0 - \gamma\beta\hat{v} + (\gamma-1)\hat{v}(\hat{v} \cdot \hat{k}_0)] \quad (9)$$

where

$$\delta = 1/[\gamma(1-\beta\hat{v} \cdot \hat{k}_0)] = 1/[\gamma(1-\beta\cos\xi)] \quad (10)$$

is the Doppler factor and  $\gamma = (1-\beta^2)^{-1/2}$  is the Lorentz factor. In the spot comoving frame photon momentum makes angle  $\alpha'$  with the local normal (see Appendix A in Poutanen & Beloborodov 2006)

$$\cos\alpha' = \delta \cos\alpha. \quad (11)$$

For rapidly rotating pulsars we need to account for the difference in light travel time around the star. Photon of impact parameter  $b$  (given by equation (4)) is lagging one with the impact parameter 0 by (Pechenick et al. 1983):

$$c\Delta t(b) = \int_R^\infty \frac{dr}{1-R_S/r} \left\{ \left[ 1 - \frac{b^2}{r^2} \left( 1 - \frac{R_S}{r} \right) \right]^{-1/2} - 1 \right\}. \quad (12)$$

A method to compute this integral accurately is given in Salmi et al. (2018). The corresponding phase delay is  $\Delta\phi = 2\pi\nu\Delta t$  and the observed phase is

$$\phi_{\text{obs}} = \phi + \Delta\phi(\phi). \quad (13)$$

For analytical calculations, the phase delays for the primary and secondary spots relative to the photons emitted from the primary spot at phase  $\phi = 0$  can be computed approximately assuming straight trajectories (Poutanen & Beloborodov 2006):

$$\Delta\phi_1(\phi) \approx 2\pi\nu R/c \sin i \sin\theta (1 - \cos\phi), \quad (14)$$

$$\Delta\phi_2(\phi) \approx 2\pi\nu R/c [2 \cos i \cos\theta + \sin i \sin\theta (1 + \cos\phi)]. \quad (15)$$

## 2.2. Observed flux and polarization degree

The combined effect of the gravitational redshift and Doppler effect results in the following relation between the monochromatic observed and local radiation intensities (see e.g. Misner et al. 1973; Rybicki & Lightman 1979):

$$I_E = \left( \frac{E}{E'} \right)^3 I'_{E'}(\alpha'), \quad (16)$$

where  $E/E' = \delta\sqrt{1-u}$ . Here  $I'_{E'}(\alpha')$  is the intensity computed in the frame comoving with the spot at energy  $E'$ . In order to compute the observed flux, we need to know variations of the solid angle occupied by the spot of area  $dS'$  in the observer's sky (Poutanen & Gierliński 2003):

$$d\Omega = \frac{dS' \cos\alpha'}{D^2} \mathcal{D} \quad (17)$$

where  $D$  is the source distance and

$$\mathcal{D} = \frac{1}{1-u} \frac{d\cos\alpha}{d\cos\psi} \quad (18)$$

is the lensing factor that can be computed numerically (Salmi et al. 2018) or using analytical approximation from Poutanen (2019). Hence the monochromatic flux becomes:

$$F_E = I_E d\Omega = (1-u)^{3/2} \delta^4 I'_{E'}(\alpha') \cos\alpha \mathcal{D} \frac{dS'}{D^2}, \quad (19)$$

where we used the aberration formula (11). Because PD does not change along photon trajectory, the observed one is equal to that measured in the spot frame at energy of the emitted photon  $E'$  and at zenith angle  $\alpha'$ :

$$P_E = P_{E'}(\alpha'). \quad (20)$$

## 2.3. Combining Stokes parameters

For each spot calculations provide us with the flux  $F_E$  computed using Eq. (19), PD  $P_E$  given by Eq. (20) and the PA  $\chi$  as derived in Sect. 3. The observed Stokes vector (we do not consider sources of circular polarization) is then

$$F_E \begin{pmatrix} 1 \\ P_E \cos 2\chi \\ P_E \sin 2\chi \end{pmatrix}. \quad (21)$$

To compute the total observed Stokes vector from two antipodal spots, we combine the Stokes parameters from each spot accounting for different time delays. The polarization degree of the total radiation is

$$P_{\text{tot}} = \frac{\sqrt{(F^p P^p)^2 + (F^s P^s)^2 + 2F^p F^s P^p P^s \cos(2\chi^p - 2\chi^s)}}{F^p + F^s}, \quad (22)$$

where superscripts p and s denote primary and secondary spot, respectively, and we skipped the energy  $E$  subscript for clarity. The total PA is given by

$$\tan(2\chi_{\text{tot}}) = \frac{F^p P^p \sin 2\chi^p + F^s P^s \sin 2\chi^s}{F^p P^p \cos 2\chi^p + F^s P^s \cos 2\chi^s}. \quad (23)$$

If the spots are extended, we can integrate over the spot surface using angular coordinates in the comoving frame (Näättilä & Pihajoki 2018; Lo et al. 2018; Bogdanov et al. 2019)

$$dS' = \gamma R^2 d\cos\theta d\phi'. \quad (24)$$

The phase dependence of the Stokes parameters for each element of the spot surface should be computed separately accounting for the difference in latitude, time delay, PA, etc.

## 3. Polarization angle

### 3.1. Rotating vector model

In order to describe polarization, we introduce the main polarization basis,

$$\hat{e}_1^m = \frac{\hat{\omega} - \cos i \hat{k}}{\sin i} = (-\cos i, 0, \sin i), \quad (25)$$

$$\hat{e}_2^m = \frac{\hat{k} \times \hat{\omega}}{\sin i} = (0, -1, 0), \quad (26)$$

where  $\hat{\omega} = (0, 0, 1)$  denotes the unit vector along the stellar rotational axis.

In the absence of relativistic rotation of the polarization plane (for a slowly rotating star), the polarization vector lies in the plane formed by the local normal  $\hat{\mathbf{n}}$  to the spot and the direction to the observer  $\hat{\mathbf{k}}$ . The corresponding polarization basis is

$$\hat{\mathbf{e}}_1 = \frac{\hat{\mathbf{n}} - \cos \psi \hat{\mathbf{k}}}{\sin \psi}, \quad \hat{\mathbf{e}}_2 = \frac{\hat{\mathbf{k}} \times \hat{\mathbf{n}}}{\sin \psi}. \quad (27)$$

The PA  $\chi_0$  measured from the projection of the spin axis on the plane of the sky in the counter-clockwise direction is given by:

$$\begin{aligned} \cos \chi_0 &= \hat{\mathbf{e}}_1^m \cdot \hat{\mathbf{e}}_1 = \hat{\mathbf{e}}_2^m \cdot \hat{\mathbf{e}}_2 = \frac{\sin i \cos \theta - \cos i \sin \theta \cos \phi}{\sin \psi}, \\ \sin \chi_0 &= \hat{\mathbf{e}}_2^m \cdot \hat{\mathbf{e}}_1 = -\hat{\mathbf{e}}_1^m \cdot \hat{\mathbf{e}}_2 = -\frac{\sin \theta \sin \phi}{\sin \psi}. \end{aligned} \quad (28)$$

We thus get the expression for the PA as in the rotating vector model (RVM) of Radhakrishnan & Cooke (1969):

$$\tan \chi_0 = \frac{\sin \theta \sin \phi}{-\sin i \cos \theta + \cos i \sin \theta \cos \phi}. \quad (29)$$

### 3.2. Rotation of PA due to rapid rotation

#### 3.2.1. PA for rapidly rotating NS ignoring bending

Now let us evaluate the effect of rapid rotation neglecting light bending, i.e. accounting for the effects of special relativity (SR) only. The photon momentum direction in the frame corotating with the spot is

$$\hat{\mathbf{k}}' = \delta \left[ \hat{\mathbf{k}} - \gamma \beta \hat{\mathbf{v}} + (\gamma - 1) \hat{\mathbf{v}} \cdot \hat{\mathbf{k}} \right] \quad (30)$$

$$= \delta \begin{pmatrix} \sin i + \sin \phi [\gamma \beta - (\gamma - 1) \cos \xi] \\ -\cos \phi [\gamma \beta - (\gamma - 1) \cos \xi] \\ \cos i \end{pmatrix}. \quad (31)$$

Following Ferguson (1973, 1976) we introduce a common vector which does not change upon Lorentz transformation from the comoving frame related to the spot and the laboratory frame related to the observer. This vector is normal to both the photon momentum and the vector of spot velocity:

$$\begin{aligned} \hat{\mathbf{M}} &= \frac{\hat{\mathbf{k}} \times \hat{\mathbf{v}}}{|\hat{\mathbf{k}} \times \hat{\mathbf{v}}|} = \frac{\hat{\mathbf{k}}' \times \hat{\mathbf{v}}}{|\hat{\mathbf{k}}' \times \hat{\mathbf{v}}|} \\ &= (-\cos i \cos \phi, -\cos i \sin \phi, \sin i \cos \phi) / \sin \xi, \end{aligned} \quad (32)$$

where  $\sin \xi = \sqrt{1 - \sin^2 i \sin^2 \phi}$ . The polarization basis related to the common vector is then

$$\hat{\mathbf{e}}_1^M = \hat{\mathbf{M}}, \quad \hat{\mathbf{e}}_2^M = \hat{\mathbf{k}} \times \hat{\mathbf{M}}. \quad (33)$$

The position angle of the projection of the common vector on the plane of the sky as measured in the main basis is

$$\cos \chi_M = \hat{\mathbf{e}}_1^m \cdot \hat{\mathbf{e}}_1^M = \frac{\cos \phi}{\sin \xi}, \quad (34)$$

$$\sin \chi_M = \hat{\mathbf{e}}_2^m \cdot \hat{\mathbf{e}}_1^M = \frac{\cos i \sin \phi}{\sin \xi}, \quad (35)$$

and then

$$\tan \chi_M = \cos i \tan \phi. \quad (36)$$

For slow rotation, the angle  $\Delta$  made by the polarization plane with the projection of the common vector on the plane of the sky is given by

$$\cos \Delta = \hat{\mathbf{e}}_1^M \cdot \hat{\mathbf{e}}_1 = \frac{-\cos i \sin \theta + \sin i \cos \theta \cos \phi}{\sin \xi \sin \psi}, \quad (37)$$

$$\sin \Delta = -\hat{\mathbf{e}}_1^M \cdot \hat{\mathbf{e}}_2 = \frac{\cos \xi \cos \psi}{\sin \xi \sin \psi} = -\frac{\sin i \sin \phi \cos \psi}{\sin \xi \sin \psi}, \quad (38)$$

and

$$\tan \Delta = \frac{\sin i \sin \phi \cos \psi}{\cos i \sin \theta - \sin i \cos \theta \cos \phi}. \quad (39)$$

It is easy to check that the PA  $\chi = \chi_M + \Delta = \chi_0$ , as given by Eq. (29).

In case of rapid rotation, the angle the polarization plane makes with the common vector should be measured in the spot comoving frame. Let us introduce the polarization basis in that frame

$$\hat{\mathbf{e}}_1' = \frac{\hat{\mathbf{n}} - \cos \psi' \hat{\mathbf{k}}'}{\sin \psi'}, \quad \hat{\mathbf{e}}_2' = \frac{\hat{\mathbf{k}}' \times \hat{\mathbf{n}}}{\sin \psi'}, \quad (40)$$

where  $\cos \psi' = \hat{\mathbf{n}} \cdot \hat{\mathbf{k}}' = \delta \cos \psi$ . Then the angle  $\Delta'$  made by the polarization plane with the projection of the common vector on the plane of the sky as seen in the comoving frame is

$$\cos \Delta' = \hat{\mathbf{e}}_1^M \cdot \hat{\mathbf{e}}_1' = \frac{-\cos i \sin \theta + \sin i \cos \theta \cos \phi}{\sin \xi \sqrt{1 - \delta^2 \cos^2 \psi}}, \quad (41)$$

$$\begin{aligned} \sin \Delta' &= -\hat{\mathbf{e}}_1^M \cdot \hat{\mathbf{e}}_2' = \frac{\cos \xi' \cos \psi}{\sin \xi \sin \psi'} \\ &= \frac{\cos \psi}{\sin \xi \sqrt{1 - \delta^2 \cos^2 \psi}} \frac{\cos \xi - \beta}{1 - \beta \cos \xi}, \end{aligned} \quad (42)$$

and

$$\tan \Delta' = \frac{\cos \psi}{\sin i \cos \theta \cos \phi - \cos i \sin \theta} \frac{\cos \xi - \beta}{1 - \beta \cos \xi}. \quad (43)$$

Thus the observed PA is the sum  $\chi = \chi_M + \Delta'$  and, using Eqs. (36) and (43), we get

$$\tan \chi = \frac{\sin \theta \sin \phi + \beta(\sin i \sin \theta + \cos i \cos \theta \cos \phi)}{-\sin i \cos \theta + \cos i \sin \theta \cos \phi - \beta \cos \theta \sin \phi}. \quad (44)$$

The deviation of the PA from that given by the nonrelativistic RVM (29) owing to only SR effect is then simply

$$\tan \chi_{c,SR} = \tan(\chi - \chi_0) = \beta \cos \psi \frac{\cos i \sin \theta - \sin i \cos \theta \cos \phi}{\sin^2 \psi + \beta \sin i \sin \phi}. \quad (45)$$

#### 3.2.2. PA for rapidly rotating NS accounting for bending in Schwarzschild metric

Because of the light bending, the photon direction close to the NS surface  $\hat{\mathbf{k}}_0$  differs from that at infinity  $\hat{\mathbf{k}}$ . Therefore, the common vector should be defined by  $\hat{\mathbf{k}}_0$  and the spot velocity vector:

$$\hat{\mathbf{M}} = \frac{\hat{\mathbf{k}}_0 \times \hat{\mathbf{v}}}{|\hat{\mathbf{k}}_0 \times \hat{\mathbf{v}}|} = \frac{\hat{\mathbf{k}}'_0 \times \hat{\mathbf{v}}}{|\hat{\mathbf{k}}'_0 \times \hat{\mathbf{v}}|} \quad (46)$$

$$= \frac{1}{\sin \xi \sin \psi} \begin{pmatrix} -\cos \phi [\cos i \sin \alpha + \cos \theta \sin(\psi - \alpha)] \\ -\sin \phi [\cos i \sin \alpha + \cos \theta \sin(\psi - \alpha)] \\ \sin i \cos \phi \sin \alpha + \sin \theta \sin(\psi - \alpha) \end{pmatrix}.$$

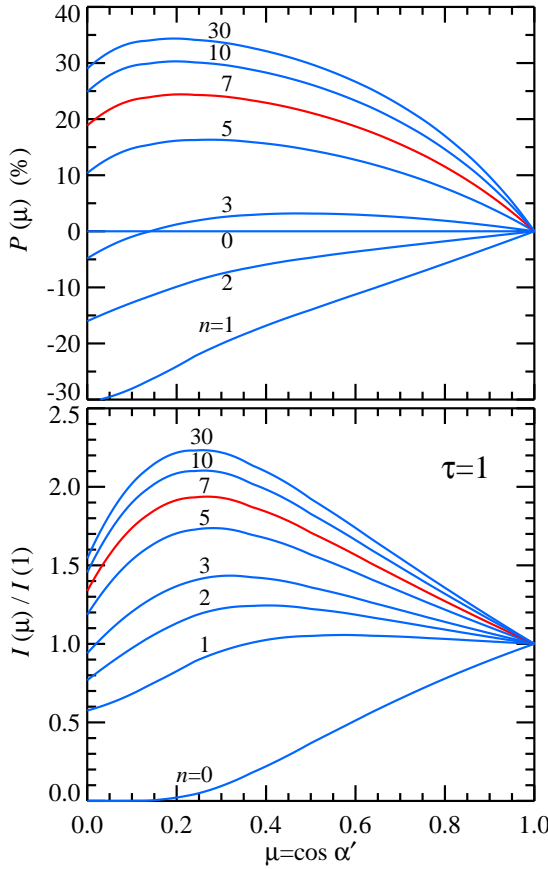


**Fig. 2.** Angular distribution of intensity (lower panel) and PD (upper panel) for different scattering orders for a slab of Thomson optical depth  $\tau = 1$ .

Let us now introduce the polarization basis related to photon momentum in the comoving frame  $\hat{k}'_0$  and the surface normal:

$$\hat{e}'_1^0 = \frac{\hat{n} - \cos \alpha' \hat{k}'_0}{\sin \alpha'}, \quad \hat{e}'_2^0 = \frac{\hat{k}'_0 \times \hat{n}}{\sin \alpha'}. \quad (47)$$

The PA of projection of vector  $\hat{M}$  on the sky as viewed in the comoving frame is

$$\cos \chi'_M = \hat{M} \cdot \hat{e}'_1^0 = \frac{\sin \alpha \sin i \cos \theta \cos \phi - \cos i \sin \theta}{\sin \psi \sin \xi \sqrt{1 - \delta^2 \cos^2 \alpha}}, \quad (48)$$

$$\begin{aligned} \sin \chi'_M &= -\hat{M} \cdot \hat{e}'_2^0 = \frac{\cos \xi' \cos \alpha}{\sin \xi \sin \alpha'} \\ &= \frac{\cos \alpha}{\sin \xi \sqrt{1 - \delta^2 \cos^2 \alpha}} \frac{\cos \xi - \beta}{1 - \beta \cos \xi}, \end{aligned} \quad (49)$$

and correspondingly

$$\tan \chi'_M = \frac{\sin \psi \cos \alpha}{\sin \alpha (\sin i \cos \theta \cos \phi - \cos i \sin \theta)} \frac{\cos \xi - \beta}{1 - \beta \cos \xi}. \quad (50)$$

Now we can evaluate the PA  $\chi_M$  of vector  $\hat{M}$  from the projection of the stellar normal on the sky as viewed in the laboratory frame. The corresponding polarization basis is

$$\hat{e}_1^0 = \frac{\hat{n} - \cos \alpha \hat{k}_0}{\sin \alpha}, \quad \hat{e}_2^0 = \frac{\hat{k}_0 \times \hat{n}}{\sin \alpha} = \hat{e}_2. \quad (51)$$

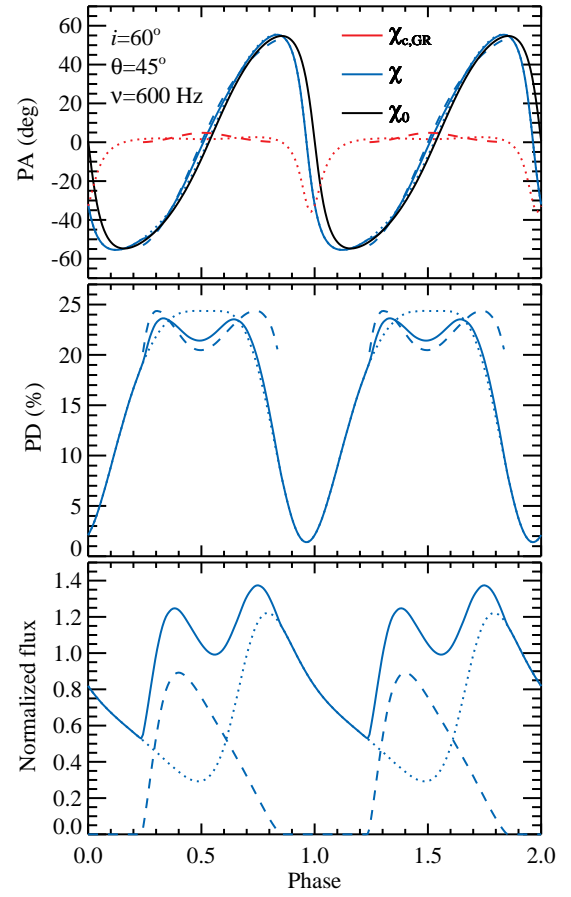


**Fig. 3.** Normalized flux (lower panel), PD (middle panel) and PA (upper panel) as a function of pulsar phase for the fiducial set of parameters  $M = 1.5M_\odot$ ,  $R = 12$  km,  $v = 600$  Hz, inclination  $i = 60^\circ$  and magnetic obliquity  $\theta = 45^\circ$ . The dotted lines show the contribution from the primary spot, the dashed lines correspond to the secondary spot, and the solid lines indicate the results for both spots. The PA  $\chi_0$  from the RVM as given by Eq. (29) for the primary spot is shown by the black line. The red lines indicate the general relativistic correction to the PA  $\chi_{c,GR}$  given by Eq. (55) for the two spots.

The equality  $\hat{e}_2^0 = \hat{e}_2$  (defined by Eq. (27)) is related to the fact that in Schwarzschild metric photon trajectories are planar. We get

$$\cos \chi_M = \hat{e}_1^0 \cdot \hat{M} = \frac{\sin i \cos \theta \cos \phi - \cos i \sin \theta}{\sin \xi \sin \psi}, \quad (52)$$

$$\sin \chi_M = \hat{e}_2^0 \cdot \hat{M} = -\frac{\cos \xi \cos \alpha}{\sin \xi \sin \alpha} = \frac{\sin i \sin \phi \cos \alpha}{\sin \xi \sin \psi}, \quad (53)$$

and

$$\begin{aligned} \tan \chi_M &= -\frac{\sin \psi \cos \alpha}{\sin \alpha (\sin i \cos \theta \cos \phi - \cos i \sin \theta)} \cos \xi \\ &= \frac{\sin i \sin \phi \cos \alpha}{\sin i \cos \theta \cos \phi - \cos i \sin \theta}. \end{aligned} \quad (54)$$

Thus because of the spot motion and light bending, the general relativistic (GR) correction to the PA,  $\chi_{c,GR} = \chi'_M + \chi_M$ , is

$$\tan \chi_{c,GR} = \beta \cos \alpha \frac{\sin \alpha \cos i \sin \theta - \sin i \cos \theta \cos \phi}{\sin \psi \sin^2 \alpha - \beta \cos \xi}. \quad (55)$$

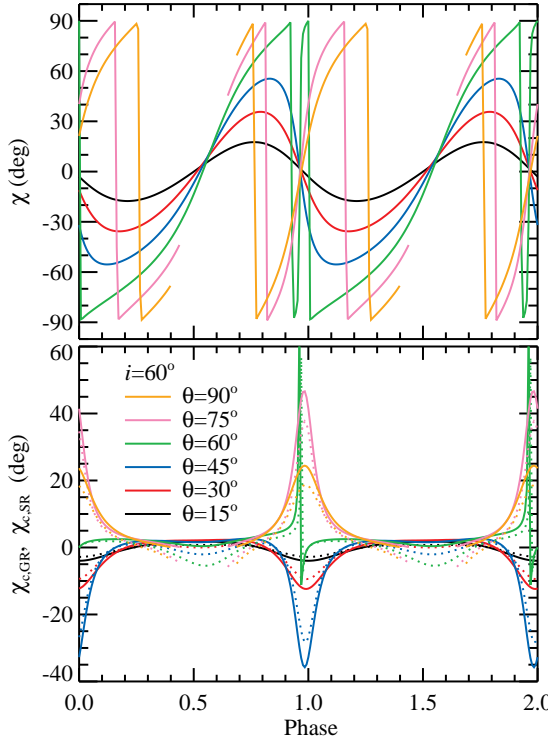


**Fig. 4.** *Upper panel:* Relativistic PA as a function of pulsar phase for one small spot at different co-latitudes  $\theta=15^\circ, 30^\circ, 45^\circ, 60^\circ, 75^\circ$ , and  $90^\circ$  shown with black, red, blue, green, pink, and orange lines, respectively. NS parameters are  $M = 1.5M_\odot$ ,  $R = 12$  km,  $\nu = 600$  Hz and inclination  $i = 60^\circ$ . The spot is not visible at some phases for  $\theta=75^\circ$  and  $90^\circ$ . *Lower panel:* Relativistic corrections to the PA. Solid lines correspond to the GR correction  $\chi_{c,GR}$ , while the dotted lines indicate the SR correction angle  $\chi_{c,SR}$ .

This coincides with expression (29) of Viironen & Poutanen (2004). The observed PA of the polarization plane relative to the projection of the stellar spin on the sky is then  $\chi = \chi_0 + \chi_{c,GR}$ :

$$\tan \chi = \frac{\sin \theta \sin \phi + \beta A}{-\sin i \cos \theta + \cos i \sin \theta \cos \phi - \beta \sin \phi C}, \quad (56)$$

where

$$\begin{aligned} A &= \frac{\sin \psi}{\sin \alpha} B + \frac{\cos \alpha - \cos \psi}{\sin \alpha \sin \psi} (\cos \phi - B \cos \psi), \\ B &= \sin i \sin \theta + \cos i \cos \theta \cos \phi, \\ C &= \frac{\sin \psi}{\sin \alpha} \cos \theta + \frac{\cos \alpha - \cos \psi}{\sin \alpha \sin \psi} (\cos i - \cos \theta \cos \psi). \end{aligned} \quad (57)$$

For slow rotation  $\beta \rightarrow 0$ , Eq. (56) transforms to Eq. (29), while if we ignore light bending, i.e. putting  $\alpha = \psi$  in Eqs. (57), the equation transforms to Eq. (44).

#### 4. Application to accreting ms pulsars

As an example of application for the developed formalism, we consider one or two antipodal small spots which emit polarized radiation. We assume that there is a plane-parallel electron-scattering dominated atmosphere of Thomson optical depth  $\tau = 1$  atop the cold NS surface. This setup may be associated with the flat accretion shock above the NS surface. Incident photons from the bottom of the slab have isotropic intensity. They are scattered

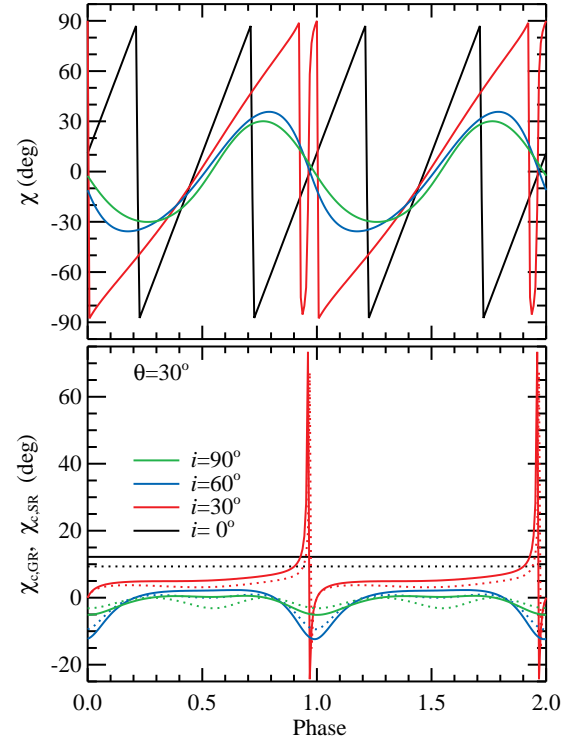


**Fig. 5.** Same as Fig. 4, but for magnetic obliquity  $\theta = 30^\circ$  and different inclinations  $i=0^\circ, 30^\circ, 60^\circ$ , and  $90^\circ$ , shown by the black, red, blue, and green lines, respectively.

multiple times in the slab. The angular distribution of the emergent radiation and its polarization characteristics are described in Viironen & Poutanen (2004). In realistic situation, the electrons in the slab are hot (according to observations  $kT_e \approx 30-70$  keV, see e.g. review in Poutanen 2006) and up-scatter incident photons to higher energies. We can associate each scattering order  $n$  with photon energy as (Rybicki & Lightman 1979)

$$E' = E_0 \left( 1 + 4 \frac{kT_e}{m_e c^2} \right)^n. \quad (58)$$

The emergent intensity and polarization degree for different scattering orders is shown in Fig. 2. Polarization degree of radiation emergent from the slab is positive if the dominant electric vector oscillations lie in the meridional plane defined by the spot normal and the direction of photon propagation, and it is negative if the oscillations are perpendicular to that plane.

Because the main emphasis of this paper is on the variation of the PA with phase and the impact of rapid rotation on PA, we just choose  $n = 7$  for illustration (see red lines in Fig. 2). This choice does not affect the PA.

We select the fiducial set of parameters:  $M = 1.5M_\odot$ ,  $R = 12$  km,  $\nu = 600$  Hz, inclination  $i = 60^\circ$  and magnetic obliquity  $\theta = 45^\circ$ . We consider infinitely small spots in most of the calculations. The dependence of the flux (normalized to unity), PD and PA on the observed pulsar phase for the fiducial set are shown in Fig. 3. For the considered geometry and NS compactness, the primary spot is visible at all phases, while the secondary spot is seen only during certain intervals. The pulse profile has a double-peak structure. The PD has a minimum when the viewing angle to the spot  $\alpha'$  is close to 0. Because the flux maximum is reached at a larger angle with  $\mu = \cos \alpha' \approx 0.2$ , the phase of the

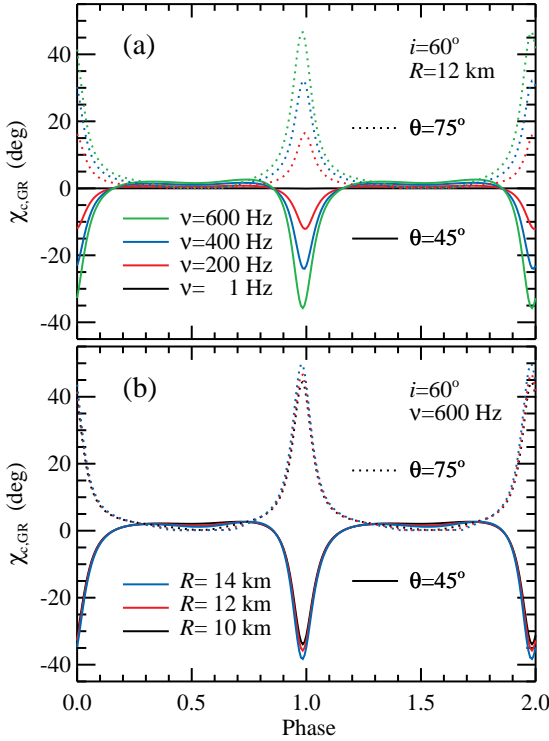


**Fig. 6.** Panel a: Phase dependence of the PA GR corrections for different NS spin rates. Black, red, blue, and green lines show results for  $v = 1, 200, 400$  and  $600$  Hz. The solid and dotted lines correspond to magnetic obliquity  $\theta = 45^\circ$  and  $75^\circ$ , respectively. Other parameters are  $M = 1.5M_\odot$ ,  $R = 12$  km, and inclination  $i = 60^\circ$ . Solid and dotted lines correspond to  $\theta = 45^\circ$  and  $75^\circ$ , respectively. Panel b: Same as panel a, but for different NS radii. Black, red, and blue lines show results for  $R = 10, 12$ , and  $14$  km for spin  $v = 600$  Hz.

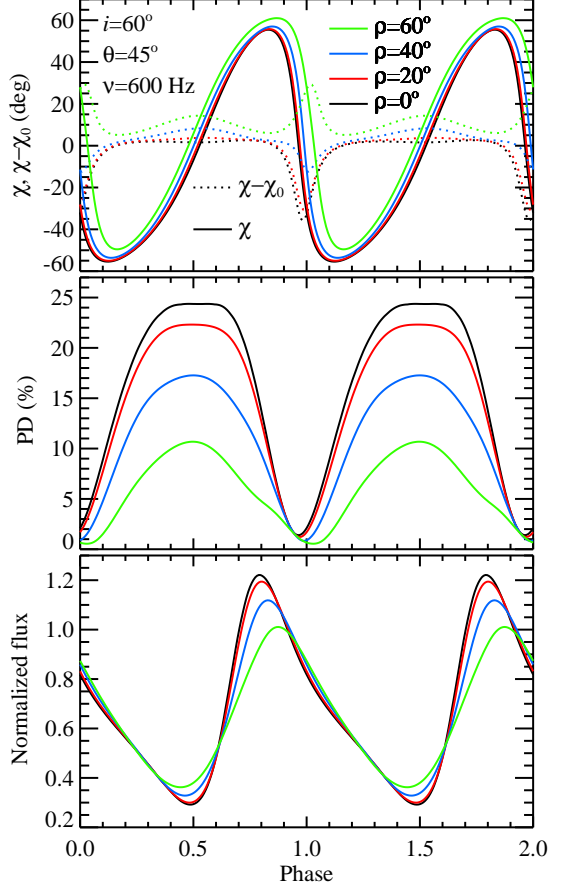


**Fig. 7.** Normalized flux (lower panel), PD (middle panel) and PA (upper panel) as a function of pulsar phase for the fiducial set of parameters for one spot of different sizes. The black, red, blue, and green lines correspond to the spot angular radius  $\rho = 0^\circ, 20^\circ, 40^\circ$ , and  $60^\circ$ . The solid lines at the upper panel show the relativistic PA  $\chi$ , while the dotted lines indicate its difference from the RVM value  $\chi_0$ .

maximum flux differs from the phase of the minimum PD. The PA follows an S-like curve. We see that additional rotation of the PA introduced by relativistic motion and light bending (red lines) reaches in this case  $40^\circ$ . The effect is largest for the primary spot, which passes close to the line connecting the observer to the NS center. In the following examples, we vary individual parameters to see the effect on the PA.

Fig. 4 shows the PA for a single spot at different magnetic obliquities  $\theta$  and fixed observer inclination. We see that for small  $\theta$ , when the spot velocity  $\beta$  is low, the correction to the PA owing to the GR effects  $\chi_{c,GR}$  is small (see bottom panel) and the total PA (top panel) is close to a sine-wave. Increasing  $\theta$  leads to a higher velocity and larger  $\chi_{c,GR}$ . The SR correction to the PA (dotted curves) has a very similar structure, but lower amplitude. The corrections are highest when  $i = \theta$  and the spot passes through the line of sight (green curves in the bottom panel). We see from Eqs. (45) and (55) that the tangent of the correction angle becomes infinite (i.e. correction angle is  $\pm\pi/2$ ) when the denominator is zero. For the SR correction, this happens at an emission phase  $\phi \approx -\beta/\sin i$ . The denominator in Eq. (55) is zero at a slightly different phase because of light bending. Approximating  $\sin \alpha/\sin \psi \approx \sqrt{1-u}$  (Poutanen & Beloborodov 2006), we get  $\phi \approx -\beta/(\sin i \sqrt{1-u})$ . The observed phase in this case is nearly the same because time delays here are computed relative to trajectories with zero impact parameter.

The phase dependencies of the PA for different inclinations and fixed  $\theta = 30^\circ$  are shown in Fig. 5. We see again that the

relativistic correction (bottom panel) can be very large when  $i = \theta$  (red lines). Interestingly, even for zero inclination (black lines) the PA does not follow the RVM dependence  $\tan \chi_0 = \tan \phi$ , but there is a shift in the PA determined by simple relations  $\chi_{c,SR} \approx \beta \cot \theta$  and  $\chi_{c,GR} \approx \beta \cot \alpha$  (where  $\alpha < \theta$  is determined by the light bending formula with  $\psi = \theta$ , see Eqs. 3–5).

Fig. 6a show the phase dependence of the GR correction to the PA for different NS spins. Obviously, for a slowly rotating star with  $v = 1$  Hz, the correction is negligibly small. It grows nearly linearly with the rotation rate as follows from Eq. (55). The sign of the correction depends on the viewing geometry. At phase  $\phi \approx 0$ , when the correction is large, it scales as  $\sin(\theta - i)$ . This results in a predominantly positive  $\chi_{c,GR}$  for  $\theta > i$  and predominantly negative for  $\theta < i$ .

Dependence of the GR correction to the PA on NS radius for a rapidly spinning star is illustrated in Fig. 6b. At higher NS radius, the velocity of the spot is higher, resulting in a larger correction, because it scales nearly linearly with  $\beta \propto R$ . The PA correction depends also on the NS compactness which influences the light bending. However, we see that the effect of the radius on  $\chi_{c,GR}$  is rather small.

All above results are obtained for an infinitely small spot. The question arises whether the PA will be affected so much by relativistic effects if the spot is large. We have computed the ob-

served flux, PD and PA for the fiducial set of parameters and varying the size of the spot from zero to  $60^\circ$ . The results are shown in Fig. 7. We note that with increasing spot size the harmonic content of the flux gets reduced. Also the PD is reduced for a larger spot by a factor of 2, because different spot elements are observed at different angles. Interestingly, the PA is affected much less. We see large deviation of the relativistic PA  $\chi$  from the values predicted by the RVM  $\chi_0$ . For the chosen set of parameters, deviations decrease up to the spot angular radius  $\rho \approx 50^\circ$ , and then they change the sign and start increasing again in absolute value.

## 5. Summary

In this paper we have developed relativistic rotating vector model. We derived exact analytic expressions for the PA observed from a spot on a rapidly rotating NS using so called common vector formalism. The expressions for PA are given when only special relativistic effects are accounted. We also derived formulae for PA accounting for the light bending in Schwarzschild metric.

We have computed relativistic PA for different inclinations and magnetic obliquities, various spin rates and NS compactnesses. We have shown that deviation of relativistic PA from the standard RVM may be very large, especially when the spot passes close to the line-of-sight towards NS center. These deviations grow nearly linearly with the spin rate but are less sensitive to the NS radius. Even for large spots, the deviations are significant and may reach tens of degrees.

The developed formalism can be applied to compute waveforms and polarization profiles from millisecond pulsars. Observations in the X-ray range with the upcoming polarimetric missions such as IXPE and eXTP will serve as a powerful tool to determine the geometry of the emission region in rapidly rotating NSs showing coherent millisecond oscillations. Combined with the waveform analysis, they may improve constraints on the NS mass and radius and the equation of state of cold dense matter.

**Acknowledgements.** This research was supported by the Russian Science Foundation grant 20-12-00364, the Academy of Finland grants 322779 and 333112, and the Magnus Ehrnrooth foundation. I thank Valery Suleimanov and Tuomo Salmi for valuable comments.

## References

Abbott, B. P., Abbott, R., Abbott, T. D., et al. 2018, Physical Review Letters, 121, 161101  
 Annala, E., Gorda, T., Kurkela, A., & Vuorinen, A. 2018, Physical Review Letters, 120, 172703  
 Antoniadis, J., Freire, P. C. C., Wex, N., et al. 2013, Science, 340, 448  
 Bauswein, A., Just, O., Janka, H.-T., & Stergioulas, N. 2017, ApJ, 850, L34  
 Beloborodov, A. M. 2002, ApJ, 566, L85  
 Bhattacharyya, S., Strohmayer, T. E., Miller, M. C., & Markwardt, C. B. 2005, ApJ, 619, 483  
 Blandford, R. D. & Königl, A. 1979, ApJ, 232, 34  
 Blaskiewicz, M., Cordes, J. M., & Wasserman, I. 1991, ApJ, 370, 643  
 Bogdanov, S. 2013, ApJ, 762, 96  
 Bogdanov, S., Grindlay, J. E., & Rybicki, G. B. 2008, ApJ, 689, 407  
 Bogdanov, S., Heinke, C. O., Öznel, F., & Güver, T. 2016, ApJ, 831, 184  
 Bogdanov, S., Lamb, F. K., Mahmoodifar, S., et al. 2019, ApJ, 887, L26  
 Braje, T. M., Romani, R. W., & Rauch, K. P. 2000, ApJ, 531, 447  
 Cadeau, C., Morsink, S. M., Leahy, D., & Campbell, S. S. 2007, ApJ, 654, 458  
 De, S., Finstad, D., Lattimer, J. M., et al. 2018, Physical Review Letters, 121, 091102  
 Demorest, P. B., Pennucci, T., Ransom, S. M., Roberts, M. S. E., & Hessels, J. W. T. 2010, Nature, 467, 1081  
 Ferguson, D. C. 1973, ApJ, 183, 977  
 Ferguson, D. C. 1976, ApJ, 205, 247  
 Fonseca, E., Pennucci, T. T., Ellis, J. A., et al. 2016, ApJ, 832, 167  
 Guillot, S., Servillat, M., Webb, N. A., & Rutledge, R. E. 2013, ApJ, 772, 7  
 Heinke, C. O., Grindlay, J. E., Lloyd, D. A., & Edmonds, P. D. 2003, ApJ, 588, 452  
 Heinke, C. O., Rybicki, G. B., Narayan, R., & Grindlay, J. E. 2006, ApJ, 644, 1090  
 Ho, W. C. G. & Heinke, C. O. 2009, Nature, 462, 71  
 Klochkov, D., Suleimanov, V., Pühlhofer, G., et al. 2015, A&A, 573, A53  
 Lattimer, J. M. & Prakash, M. 2007, Phys. Rep., 442, 109  
 Lattimer, J. M. & Steiner, A. W. 2014, ApJ, 784, 123  
 Leahy, D. A., Morsink, S. M., & Cadeau, C. 2008, ApJ, 672, 1119  
 Leahy, D. A., Morsink, S. M., Chung, Y.-Y., & Chou, Y. 2009, ApJ, 691, 1235  
 Lo, K. H., Miller, M. C., Bhattacharyya, S., & Lamb, F. K. 2013, ApJ, 776, 19  
 Lo, K. H., Miller, M. C., Bhattacharyya, S., & Lamb, F. K. 2018, ApJ, 854, 187  
 Lorimer, D. R. 2008, Living Reviews in Relativity, 11 [arXiv:0811.0762]  
 Lyutikov, M. 2016, ArXiv e-prints [arXiv:1607.00777]  
 Lyutikov, M. 2017, Phys. Rev. D, 95, 124003  
 Lyutikov, M. & Kravchenko, E. V. 2017, MNRAS, 467, 3876  
 Lyutikov, M., Pariev, V. I., & Blandford, R. D. 2003, ApJ, 597, 998  
 Miller, M. C., Chirenti, C., & Lamb, F. K. 2020, ApJ, 888, 12  
 Miller, M. C. & Lamb, F. K. 2015, ApJ, 808, 31  
 Miller, M. C., Lamb, F. K., Dittmann, A. J., et al. 2019, ApJ, 887, L24  
 Misner, C. W., Thorne, K. S., & Wheeler, J. A. 1973, Gravitation (San Francisco: W.H. Freeman and Co.)  
 Morsink, S. M. & Leahy, D. A. 2011, ApJ, 726, 56  
 Morsink, S. M., Leahy, D. A., Cadeau, C., & Braga, J. 2007, ApJ, 663, 1244  
 Most, E. R., Weih, L. R., Rezzolla, L., & Schaffner-Bielich, J. 2018, Physical Review Letters, 120, 261103  
 Nättilä, J., Miller, M. C., Steiner, A. W., et al. 2017, A&A, 608, A31  
 Nättilä, J. & Pihajoki, P. 2018, A&A, 615, A50  
 Nättilä, J., Steiner, A. W., Kajava, J. J. E., Suleimanov, V. F., & Poutanen, J. 2016, A&A, 591, A25  
 Öznel, F. & Freire, P. 2016, ARA&A, 54, 401  
 Öznel, F., Güver, T., & Psaltis, D. 2009, ApJ, 693, 1775  
 Pavlov, G. G. & Zavlin, V. E. 2000, ApJ, 529, 1011  
 Pechenick, K. R., Ftaclas, C., & Cohen, J. M. 1983, ApJ, 274, 846  
 Poutanen, J. 2006, Advances in Space Research, 38, 2697  
 Poutanen, J. 2019, arXiv e-prints, arXiv:1909.05732  
 Poutanen, J. & Beloborodov, A. M. 2006, MNRAS, 373, 836  
 Poutanen, J. & Gierliński, M. 2003, MNRAS, 343, 1301  
 Poutanen, J., Nättilä, J., Kajava, J. J. E., et al. 2014, MNRAS, 442, 3777  
 Radhakrishnan, V. & Cooke, D. J. 1969, Astrophys. Lett., 3, 225  
 Riley, T. E., Watts, A. L., Bogdanov, S., et al. 2019, ApJ, 887, L21  
 Rutledge, R. E., Bildsten, L., Brown, E. F., Pavlov, G. G., & Zavlin, V. E. 1999, ApJ, 514, 945  
 Rybicki, G. B. & Lightman, A. P. 1979, Radiative processes in astrophysics (New York: Wiley-Interscience)  
 Salmi, T., Nättilä, J., & Poutanen, J. 2018, A&A, 618, A161  
 Steiner, A. W., Heinke, C. O., Bogdanov, S., et al. 2018, MNRAS, 476, 421  
 Steiner, A. W., Lattimer, J. M., & Brown, E. F. 2010, ApJ, 722, 33  
 Steiner, A. W., Lattimer, J. M., & Brown, E. F. 2013, ApJ, 765, L5  
 Stevens, A. L., Feige, J. D., Leahy, D. A., & Morsink, S. M. 2016, ApJ, 833, 244  
 Suleimanov, V., Poutanen, J., Revnivtsev, M., & Werner, K. 2011, ApJ, 742, 122  
 Suleimanov, V. F., Klochkov, D., Poutanen, J., & Werner, K. 2017, A&A, 600, A43  
 Suleimanov, V. F., Poutanen, J., & Werner, K. 2020, A&A, in press, arXiv:2005.09759  
 Viironen, K. & Poutanen, J. 2004, A&A, 426, 985  
 Watts, A. L., Andersson, N., Chakrabarty, D., et al. 2016, Reviews of Modern Physics, 88, 021001  
 Watts, A. L., Yu, W., Poutanen, J., et al. 2019, Science China Physics, Mechanics, and Astronomy, 62, 29503  
 Webb, N. A. & Barret, D. 2007, ApJ, 671, 727  
 Weisskopf, M. C., Ramsey, B., Ö'Dell, S., et al. 2016, in Proc. SPIE, Vol. 9905, Space Telescopes and Instrumentation 2016: Ultraviolet to Gamma Ray, 990517  
 Zhang, S., Santangelo, A., Feroci, M., et al. 2019, Science China Physics, Mechanics, and Astronomy, 62, 29502  
 Zhang, S. N., Feroci, M., Santangelo, A., et al. 2016, in Proc. SPIE, Vol. 9905, Space Telescopes and Instrumentation 2016: Ultraviolet to Gamma Ray, 99051Q